Chinese Chemical Letters 35 (2024) 108552

Contents lists available at ScienceDirect

Chinese Chemical Letters

journal homepage: www.elsevier.com/locate/cclet

Engineering and understanding $SnS_{0.5}Se_{0.5}$@N/S/Se triple-doped carbon nanofibers for enhanced sodium-ion batteries

Fanjun Kong[a,c], Yixin Ge[a], Shi Tao[a,*], Zhengqiu Yuan[c], Chen Lu[a], Zhida Han[a], Lianghao Yu[b,*], Bin Qian[a,*]

[a] *School of Electronic and Information Engineering, Changshu Institute of Technology, Changshu 215500, China*
[b] *Key Laboratory of Spin Electron and Nanomaterials of Anhui Higher Education Institutes, Suzhou University, Suzhou 234000, China*
[c] *Far East Holding Group Co., Ltd., Yixing 214200, China*

ARTICLE INFO

Article history:
Received 27 February 2023
Revised 30 March 2023
Accepted 8 May 2023
Available online 11 May 2023

Keywords:
$SnS_{0.5}Se_{0.5}$
Carbon nanofibers
Doping
Density functional theory
Sodium ion batteries

ABSTRACT

Tin-based chalcogenides have attracted tremendous attention as an anode material for sodium storage owing to their unique structure and high theoretical capacity. Unfortunately, the large volume change and poor conductivity lead to sluggish reaction kinetics and poor cycling performance. Herein, $SnS_{0.5}Se_{0.5}$ nanoparticles coupled with N/S/Se triple-doped carbon nanofibers ($SnS_{0.5}Se_{0.5}$@NSSe-C) are designed and synthesized through electrospinning and annealing process. Benefiting from the synergistic effects of $SnS_{0.5}Se_{0.5}$ and NSSe-C, the $SnS_{0.5}Se_{0.5}$@NSSe-C nanofibers exhibit a high reversible capacity and ultralong cycle life at higher current density for sodium-ion batteries. Furthermore, the sodium storage mechanism and electrochemical reaction kinetics of the $SnS_{0.5}Se_{0.5}$@NSSe-C composite are characterized by the *in-situ* measurements. The theoretical calculations further reveal the structural advantages of $SnS_{0.5}Se_{0.5}$@NSSe-C composite, which exhibits a high adsorption energy of Na^+. This work can provide a novel idea for the synthesis of ternary tin-based chalcogenides and is beneficial for the investigation of their reaction kinetics.

Transition metal chalcogenides (TMCs) have attracted extensive scientific interest in the fields of electrochemical energy storage and conversion due to their unique chemical and physical properties [1–3]. In particular, ternary tin-based chalcogenides (SnSSe) deliver the high theoretical capacity based on the multiple ion storage mechanisms and appropriate voltage plateaus, and their layered structure with large interlayer spacing is conducive to the insertion of alkali (Li, Na, K) ion storage and alleviate volume expansion [4–6]. However, SnSSe exhibits the deficient kinetics and fast capacity decay during the discharge and charge process, owing to its unsatisfactory electronic/ionic conductivity, and serious structural degradation and volume change. Therefore, many strategies including nanostructure design, nanocomposite optimization, doping and heterojunction *etc.* have been designed to enhance the ion storage performance of anode materials [7–10]. Specially, various carbon substrates with different morphologies are often used to improve conductivity, reduce diffusion distance, sustain structural strain and accommodate volume expansion of electrodes.

As a kind of carbon substrates, carbon nanofibers (CNF) with one-dimensional structure, good electrical conductivity, high mechanical strength and low density, have been applied to enhance the sodium storage performance of TMCs [11,12]. The unique structure of CNF can provide high surface-volume ratios, facilitate rapid electron/ion transport and enhance the stability of electrodes. Although CNF can improve the electrochemical performance of tin-based electrodes, designing the ternary tin-based chalcogenides coupled with CNF is rarely reported, many works do not pay attention to the synergistic effects and reaction mechanism on the hybrid composites. Meanwhile, heteroatom doping has been explored to be an effective method to introduce external defect, generate rich active sites and further optimize electronic conductivity of CNF [13].

Herein, we designed and prepared the ternary tin selenium sulfide ($SnS_{0.5}Se_{0.5}$) nanoparticles coupled with N/S/Se triple-doped carbon nanofibers (NSSe-C) through a facile strategy for the first time. Combined the merits of high theoretical capacity of $SnS_{0.5}Se_{0.5}$, and high conductivity and stability of NSSe-C, $SnS_{0.5}Se_{0.5}$@NSSe-C nanofibers display the improved sodium storage performance. Moreover, the reaction mechanisms and kinetics of $SnS_{0.5}Se_{0.5}$@NSSe-C nanofibers are investigated in detail though in situ methods and theoretical calculations.

---

* Corresponding authors.
E-mail addresses: taoshi@cslg.edu.cn (S. Tao), lhyu@ahszu.edu.cn (L. Yu), njqb@cslg.edu.cn (B. Qian).

https://doi.org/10.1016/j.cclet.2023.108552
1001-8417/

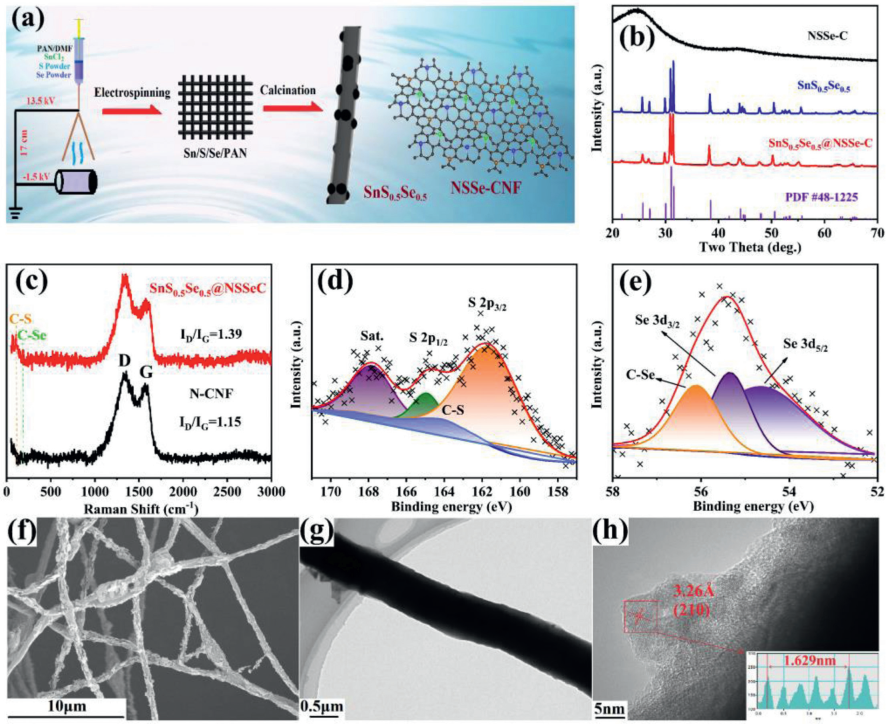

Fig. 1. (a) Schematic illustration of the preparation of $SnS_{0.5}Se_{0.5}$@NSSe-C. (b) XRD patterns of $SnS_{0.5}Se_{0.5}$, NSSe-C and $SnS_{0.5}Se_{0.5}$@NSSe-C. (c) Raman spectra of N—CNF and $SnS_{0.5}Se_{0.5}$@NSSe-C. XPS spectra of the $SnS_{0.5}Se_{0.5}$@NSSe-C: (d) S 2p and (e) Se 3d, (f) TEM and (g, h) HRTEM images of $SnS_{0.5}Se_{0.5}$@NSSe-C.

The two-step preparation of $SnS_{0.5}Se_{0.5}$@NSSe-C composite is illustrated in Fig. 1a. In the synthesis process of $SnS_{0.5}Se_{0.5}$ active material, multi-element doping of carbon fiber were achieved. Fig. 1b shows XRD patterns of $SnS_{0.5}Se_{0.5}$ prepared by solid state method, and $SnS_{0.5}Se_{0.5}$@NSSe-C and NSSe-C prepared by electrospinning and heat treatment process. The characteristic diffraction peaks of $SnS_{0.5}Se_{0.5}$ and $SnS_{0.5}Se_{0.5}$@NSSe-C are corresponding exactly to the indexed $SnS_{0.5}Se_{0.5}$ (PDF#48–1225 [14]), suggesting good crystallinity and high purity. In Fig. S1 (Supporting information), the synthesis of $SnS_{0.5}Se_{0.5}$@NSSe-C nanofibers require more sulfur and selenium powders to avoid the formation of Sn impurity, and additional sulfur and selenium powders can be doped into the N—CNF, creating more defects. The two definite peaks between 1200 cm^{-1} and 1700 cm^{-1} are observed in the Raman spectra of N—CNF and $SnS_{0.5}Se_{0.5}$@NSSe-C (Fig. 1c). The peak intensity ratio of disordered amorphous carbon (D bond) and crystalline graphic carbon (G bond) (I_D/I_G) value of $SnS_{0.5}Se_{0.5}$@NSSe-C (1.39) is higher than that of pure N—CNF (1.15), indicating that the S/Se doping can create more structural defects and vacancies in N—CNF, which can provide additional electrochemical action sites and help to accelerate sodium diffusion. The two peaks at 190 and 780 cm^{-1} for $SnS_{0.5}Se_{0.5}$@NSSe-C correspond to the C-Se and C-S bonds, respectively, which suggesting the existence of S/Se doping into the N—CNF [15,16]. Fig. S2 (Supporting information) shows the TGA/DSC curves of the $SnS_{0.5}Se_{0.5}$@NSSe-C and two exothermic peaks at 123 and 512 °C are observed, which are related to the evaporation of physically adsorbed water and the oxidation of $SnS_{0.5}Se_{0.5}$@NSSe-C, respectively. Based the residual mass, the carbon content in $SnS_{0.5}Se_{0.5}$@NSSe-C can be calculated to 45.63%. The XPS characteristic peaks corresponding Sn, S, Se and N elements are observed in Fig. S3 (Supporting information) and the N element is mainly produced by carbonization of polypropylene. As shown in Fig. S4 (Supporting information), the three fitted peaks located at 398.4, 399.8 and 400.5 eV correspond to pyridinic-N, pyrrolic-N and graphitic-N, respectively [17,18]. The high-resolution C 1s spectrum in Fig. S5 (Supporting information) can be fitted and separated into five peaks at 284.5, 284.9, 285.7, 286.5 and 288.6 eV, attributing to C—C/C=C, C—O, C—N, C-S/Se and O—C=O bonds, respectively [19]. The C-S/Se bond can prove the partial substitution of carbon with S and Se elements, increasing the disorder degree of graphitization. The two peaks at 161.6 and 164.9 eV in Fig 1d correspond to S $2p_{3/2}$ and S $2p_{1/2}$, respectively, and the other peaks at 164.1 and 167.8 eV are ascribed to the C-S bond and satellite peak [20]. In the Se 3d spectra (Fig. 1e), three peaks are observed at 54.6, 55.3 and 56.1 eV, ascribed to the Se $3d_{5/2}$, Se $3d_{3/2}$ and C-Se bond, respectively [21].

Fig. S6 (Supporting information) shows the morphology of $SnS_{0.5}Se_{0.5}$ prepared by solid state method, which displays the irregular shape of several microns. Benefiting from the continuous frame structure of NSSe-C (Fig. S7 in Supporting information), the $SnS_{0.5}Se_{0.5}$@NSSe-C can maintain the fibrous structure morphology in Fig. 1f and $SnS_{0.5}Se_{0.5}$ particles with several hundred nanometers are embedded into the N/S/Se triple-doped carbon nanofibers in Fig. S8 (Supporting information). The microstructure of $SnS_{0.5}Se_{0.5}$@NSSe-C nanofibers is exhibited in Fig. 1g and the interior are solid structure. In the HRTEM image of $SnS_{0.5}Se_{0.5}$@NSSe-C nanofibers (Fig. 1h), the clear lattice fringe of 3.26 Å is observed, which is related to the (210) plane of $SnS_{0.5}Se_{0.5}$. Moreover, the TEM elemental mapping images of $SnS_{0.5}Se_{0.5}$@NSSe-C nanofibers in Fig. S9 (Supporting information) illustrate the homogeneous distribution of Sn, S, Se, N and C elements, further confirming the successful formation of the $SnS_{0.5}Se_{0.5}$@NSSe-C nanofibers.

The *in-situ* XRD tests were carried out to reveal the sodium storage mechanism of $SnS_{0.5}Se_{0.5}$@NSSe-C nanofibers. In Fig. 2a, the intensity of the diffraction peak increases as the color changes from purple to red. The diffraction peaks corresponding to the (111) and (400) planes significantly shift to higher angles at initial discharge states (Fig. S10 in Supporting information), indicating the sodium ions insertion into the lattice with formation of $Na_xSnS_{0.5}Se_{0.5}$. As continuous discharge, the characteristic peaks of

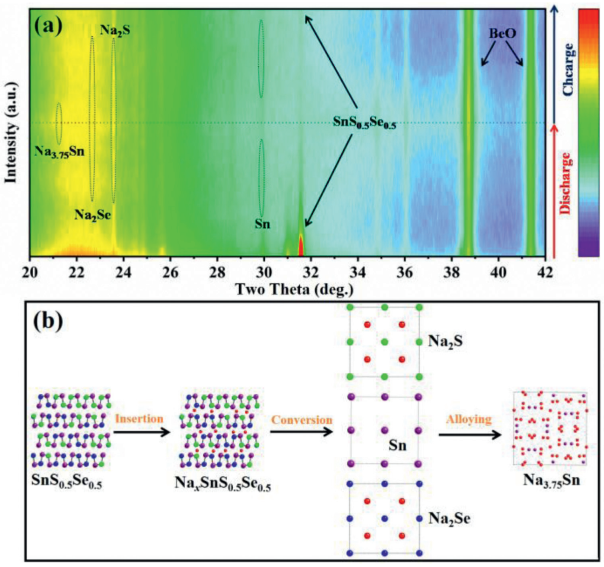

Fig. 2. (a) *In-situ* XRD patterns of $SnS_{0.5}Se_{0.5}$@NSSe-C nanofibers in the first cycle and (b) the schematic diagram of sodium storage mechanism of $SnS_{0.5}Se_{0.5}$ electrode.

Sn, Na_2S and Na_2Se phases are observed, corresponding to the conversion reaction of $Na_xSnS_{0.5}Se_{0.5}$. When discharged to the 0.1 V, the formation of $Na_{3.75}Sn$ is related to the alloying reaction of Sn and observed in the HRTEM image (Fig. S11 in Supporting information) [22]. During the charge process, the weak diffraction peaks of $SnS_{0.5}Se_{0.5}$ gradually appear, implying a certain reversibility of the structure. The characteristic planes of Na_2S and Na_2Se intermediates still exist after the charge process, which is attributed to the loss of electrochemical activity of some sodium ions to maintain structural stability. Thus, the sodium storage mechanism of $SnS_{0.5}Se_{0.5}$ can be summarized as Fig. 2b, which is composed of insertion, conversion and alloying reactions.

As shown in Fig. S12 (Supporting information), the three reduction peaks in the initial scan for $SnS_{0.5}Se_{0.5}$ are observed at 1.01, 0.65 and 0.14 V, corresponding to the Na^+ insertion into the $SnS_{0.5}Se_{0.5}$ layer, the conversion reaction of $Na_xSnS_{0.5}Se_{0.5}$ and structural activation process, and the alloying reaction of Sn, respectively. Meanwhile, the three oxidation peaks at 0.28, 0.91 and 1.04 V in the anodic scan are attributed to the desodiation process ($Na_{3.75}Sn \rightarrow Sn \rightarrow Na_xSnS_{0.5}Se_{0.5} \rightarrow SnS_{0.5}Se_{0.5}$). Compared with curves of $SnS_{0.5}Se_{0.5}$, the redox process of $SnS_{0.5}Se_{0.5}$@NSSe-C nanofibers is relatively gentle in the presence of NSSe-C, suggesting that the NSSe-C can prevent the large volume changes of active materials. In Fig. S13 (Supporting information), the subsequent CV curves (2^{nd} to 5^{th}) of $SnS_{0.5}Se_{0.5}$ are completely different, and some redox peaks shift or even disappear, which is ascribed to the irreversible decomposition of $SnS_{0.5}Se_{0.5}$ caused by the volume changes. On the contrary, the following CV curves of NSSe-C almost coincide in Fig. S14 (Supporting information) with excellent electrochemical reversibility. Meanwhile, Fig. 3a presents the reproducible curves of $SnS_{0.5}Se_{0.5}$@NSSe-C nanofibers, demonstrating the superior reversibility of sodiation/desodiation behavior of $SnS_{0.5}Se_{0.5}$@NSSe-C nanofibers. As displayed in Fig. S15 (Supporting information), the initial discharge and charge capacities of $SnS_{0.5}Se_{0.5}$, NSSe-C and $SnS_{0.5}Se_{0.5}$@NSSe-C nanofibers are 794.5/566.4, 448.8/214.8 and 1123.8/676.7 mAh/g at 0.1 A/g, respectively. The high discharge capacity of $SnS_{0.5}Se_{0.5}$@NSSe-C nanofibers is attributed to multiple reaction mechanisms of $SnS_{0.5}Se_{0.5}$ and the generation of solid electrolyte interphase (SEI) with more sodium ions consumption [23]. In addition, the irreversible capacity loss is mainly owing to some irreversible structural changes of $SnS_{0.5}Se_{0.5}$ and low coulombic efficiency of NSSe-C. The cycling performance of $SnS_{0.5}Se_{0.5}$, NSSe-C and $SnS_{0.5}Se_{0.5}$@NSSe-C nanofibers was evaluated at 0.1 A/g and exhibited in Fig. 3b. Obviously, the $SnS_{0.5}Se_{0.5}$ particles present the rapid capacity fading and a low capacity of 25.4 mAh/g after 100 cycles. The low conductivity and large volume expansion of $SnS_{0.5}Se_{0.5}$ may lead to the poor cycling ability with severe pulverization. Moreover, the NSSe-C nanofibers play excellent cycling stability during discharge and charge process. To determine the effect of S/Se doping on the N−CNF, the cycling and rate performance of N−CNF were tested and shown in Fig. S16 (Supporting information). The cycling capacity of NSSe-C nanofibers is higher than that of the pure N−CNF, indicating that the S/Se doping can improve the electrochemical activity of the pure N−CNF. Profiting from the high theoretical capacity of $SnS_{0.5}Se_{0.5}$ and high conductivity of the NSSe-C nanofibers, the $SnS_{0.5}Se_{0.5}$@NSSe-C nanofibers can maintain a reversible capacity of 478.8 mAh/g, much higher than the capacity of $SnS_{0.5}Se_{0.5}$. Fig. 3c compares the rate performance of $SnS_{0.5}Se_{0.5}$, NSSe-C and $SnS_{0.5}Se_{0.5}$@NSSe-C nanofibers, and the specific capacities of the $SnS_{0.5}Se_{0.5}$@NSSe-C are higher than the values of $SnS_{0.5}Se_{0.5}$and NSSe-C at various current densities. A comparison of the cycling performance of $SnS_{0.5}Se_{0.5}$@NSSe-C nanofibers for SIBs with some reported TMCs is listed in Table S1 (Supporting information) and $SnS_{0.5}Se_{0.5}$@NSSe-C nanofibers show the better sodium storage performance. Furthermore, Fig. S17 (Supporting information) shows the long cycling performance of $SnS_{0.5}Se_{0.5}$@NSSe-C nanofibers at 2.0 A/g. After five cycles at 0.1 A/g, the $SnS_{0.5}Se_{0.5}$@NSSe-C can reach a high capacity of 225.0 mAh/g after 2000 cycles, indicating the outstanding rate capability of the $SnS_{0.5}Se_{0.5}$@NSSe-C nanofibers. As presented in Fig. S18 (Supporting information), the $SnS_{0.5}Se_{0.5}$@NSSe-C with low carbon content delivers the better cycling performance than that with high carbon content, which is attributed to that more carbon content can reduce the amount of active material. It was found that no fibrous precursor was formed when the ratio of raw material (Sn:S:Se) exceeded 4:6:6. Thus, the ratio of 4:6:6 can be the best ratio to enhance the cycling capacity of $SnS_{0.5}Se_{0.5}$@NSSe-C.

To further illuminate the excellent rate capability and electrochemical reaction kinetics of $SnS_{0.5}Se_{0.5}$@NSSe-C nanofibers, the CV tests were performed from 0.1 mV/s to 2.0 mV/s and displayed in Fig. S19 (Supporting information). According to the previous studies [24,25], the relationship between the current (i) and the scan rate (v) can be expressed as the following formulas:

$$i = av^b \tag{1}$$

$$\log(i) = b\log(v) + \log(a) \tag{2}$$

The calculated b values of peaks for $SnS_{0.5}Se_{0.5}$@NSSe-C nanofibers in Fig. S20 (Supporting information) are between 0.5 and 1.0, indicating that the reaction kinetics include the diffusion-controlled and capacitive behavior. Furthermore, the reaction kinetics are quantitatively analyzed by the following equation:

$$i = k_1v + k_2v^{1/2} \tag{3}$$

As revealed in Fig. 3d, the capacitive contributions of $SnS_{0.5}Se_{0.5}$@NSSe-C nanofibers are 42.2%, 45.2%, 53.6%, 66.2% and 82.2% at 0.1, 0.2, 0.5, 1.0 and 2.0 mV/s, respectively, high than those of $SnS_{0.5}Se_{0.5}$ (Fig. S21 in Supporting information). The high capacitive contribution leads to the fast charge transfer behavior, which is favorable for high rate and long cycling performance of sodium storage [26,27].

To better illustrate the extraordinary sodium storage performance of $SnS_{0.5}Se_{0.5}$@NSSe-C nanofibers, the GITT method was applied in Fig. S22 (Supporting information). The D_{Na+} values of $SnS_{0.5}Se_{0.5}$@NSSe-C nanofibers can be obtained according to the

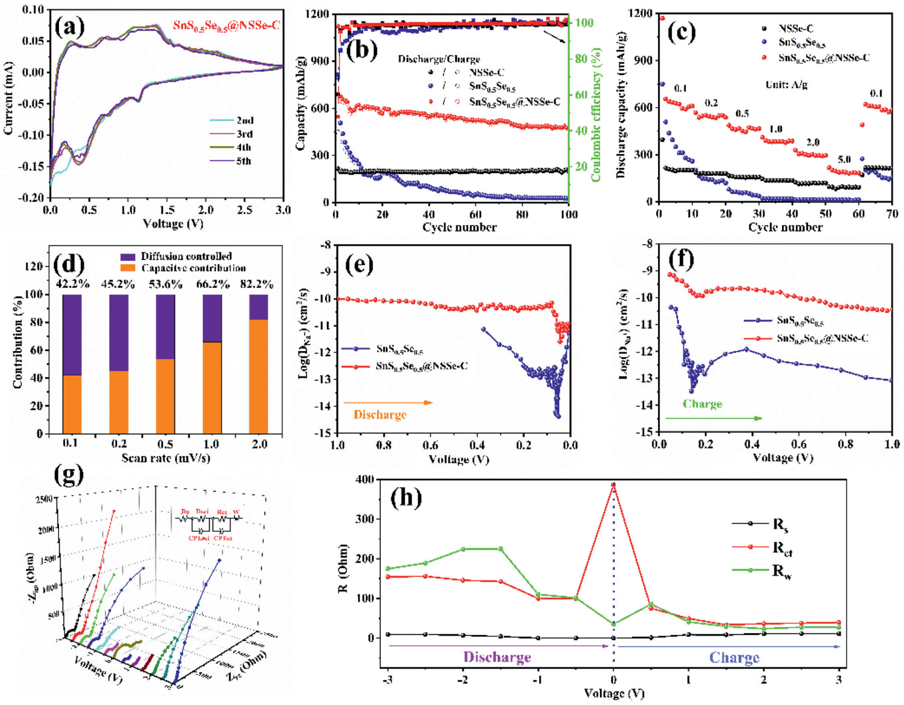

Fig. 3. (a) CV curves of $SnS_{0.5}Se_{0.5}$@NSSe-C. (b) Cycling performance, (c) rate performance of $SnS_{0.5}Se_{0.5}$, NSSe-C and $SnS_{0.5}Se_{0.5}$@NSSe-C. (d) Capacitive contribution ratio at various scan rates of $SnS_{0.5}Se_{0.5}$@NSSe-C. The diffusion coefficients at (e) discharging and (f) charging states of $SnS_{0.5}Se_{0.5}$ and $SnS_{0.5}Se_{0.5}$@NSSe-C. (g) *In-situ* Nyquist plots and (h) the resistances corresponding to the *in-situ* Nyquist plots of $SnS_{0.5}Se_{0.5}$@NSSe-C.

following equation [28]:

$$D_{Na^+} = \frac{4}{\pi t}\left(\frac{mV_M}{MA}\right)^2\left(\frac{\Delta E_s}{\Delta E_t}\right)^2 \tag{4}$$

During the initial sodiation process (Fig. 3e), the D_{Na^+} of $SnS_{0.5}Se_{0.5}$ drops slowly, attributed to that the deepening of conversion reaction can lead to the decrease in the sodium requirement. Interestingly, the alloying reaction results in the increase of the D_{Na^+} approaching 0.01 V. As shown in Fig. 3f, the D_{Na^+} displays a completely opposite change, which corresponds to the alloying and conversion reactions in the desodiation process. Compared to the D_{Na^+} of $SnS_{0.5}Se_{0.5}$, $SnS_{0.5}Se_{0.5}$@NSSe-C nanofibers present the more table diffusion process and higher D_{Na^+} values, suggesting that the introduction of NSSe-C nanofibers can solve the problems of slow ion diffusion caused by volume expansion and poor conductivity of $SnS_{0.5}Se_{0.5}$.

The sodium ion transfer kinetics and interfacial stability were investigated by EIS measurement [29]. Fig. S23 (Supporting information) exhibits the typical Nyquist plots of $SnS_{0.5}Se_{0.5}$, $SnS_{0.5}Se_{0.5}$@NSSe-C and NSSe-C after 100 cycles, which can be fitted by equivalent circuit. The R_s, R_{ct} and R_w represent the solvent resistance, charge transfer resistance and diffusion resistance, respectively [30]. The R_{ct} value of $SnS_{0.5}Se_{0.5}$@NSSe-C nanofibers is 154.6 Ω, higher than that of $SnS_{0.5}Se_{0.5}$ (667.1 Ω) and lower than that of NSSe-C (85.69 Ω), indicating that the high conductivity and continuous network structure of NSSe-C can shorten the diffusion distance and accelerate the charge transfer of pure $SnS_{0.5}Se_{0.5}$ particles. Moreover, the detailed *in-situ* Nyquist plots are shown in Fig. 3g and the corresponding impedance values are displayed in Fig. 3h. Notably, the R_s value keeps a relative stability during cycling process owing to the stable formation of SEI films. Before sodiation to 0.5 V, the R_{ct} value decreases slowly with the depth of discharge, which is attributed to that the Sn element generated by the conversion reaction can improve the electrical conductivity and facilitate the charge transfer. However, the structural change caused by the alloying reaction and the decrease of Sn element can lead to the sluggish charge transfer and increase of the R_{ct} value at 0.01 V. The R_w value increase at initial discharge states, which is related to the increase of interlayer spacing and internal stress caused by insertion reaction. Then, the R_w value decreases with decrease of voltage, ascribed to that subsequent conversion and alloying reactions can continue to react with sodium ions and enhance the diffusion kinetics. The R_{ct} and R_w values show similar opposite changes during the desodiation process, indicating the excellent reversibility of charge transport and ion diffusion kinetics of $SnS_{0.5}Se_{0.5}$@NSSe-C nanofibers.

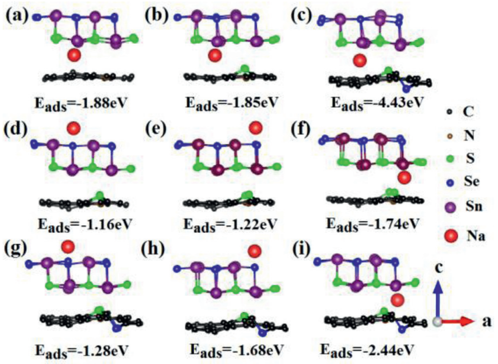

Fig. 4. Geometries of the optimized (a) $SnS_{0.5}Se_{0.5}$@N−C, (b) $SnS_{0.5}Se_{0.5}$@NS-C and (c) $SnS_{0.5}Se_{0.5}$@NSSe-C at the same sodium atom adsorption sites. Geometries of the optimized (d-f) $SnS_{0.5}Se_{0.5}$@NS-C and (g-i) $SnS_{0.5}Se_{0.5}$@NSSe-C at the different sodium atom adsorption sites.

The DFT calculations were performed to reveal the structural advantages of $SnS_{0.5}Se_{0.5}$@NSSe-C nanofibers. As displayed in Figs. 4a-c, the adsorption energy (E_{ads}) between Na^+ and $SnS_{0.5}Se_{0.5}$@N−C, $SnS_{0.5}Se_{0.5}$@NS-C or $SnS_{0.5}Se_{0.5}$@NSSe-C at same adsorption sites is calculated to be −1.88, −1.85 and −4.43 eV, respectively, indicating the stronger interaction of $SnS_{0.5}Se_{0.5}$ adsorption on NSSe-C. The higher negative adsorption energy illustrates more electrochemical active site in the $SnS_{0.5}Se_{0.5}$@NSSe-C, which are beneficial for sodium storage performance [31,32]. The E_{ads} between Na^+ and $SnS_{0.5}Se_{0.5}$@NS-C or $SnS_{0.5}Se_{0.5}$@NSSe-C at the different adsorption sites is further calculated and presented in Figs. 4d-i. The $SnS_{0.5}Se_{0.5}$@NSSe-C composite delivers the better Na^+ adsorption performance than $SnS_{0.5}Se_{0.5}$@NS-C, demonstrating great sodium storage potential. The results also prove that the interlayer between $SnS_{0.5}Se_{0.5}$ and NSSe-C is more conducive to sodium ion insertion.

In summary, the $SnS_{0.5}Se_{0.5}$ nanoparticles coupled with N/S/Se triple-doped carbon nanofibers ($SnS_{0.5}Se_{0.5}$@NSSe-C) have been synthesized through two-step process, and investigated as an anode material for SIBs. Due to the synergistic effect of $SnS_{0.5}Se_{0.5}$ and NSSe-C, the $SnS_{0.5}Se_{0.5}$@NSSe-C composite delivers superior sodium storage performance with ultralong cycle life at a high current density and fast reaction kinetics. This work can provide an intelligent strategy for the efficient construction of high-performance electrodes with fast electrochemical reaction kinetics and increase the understanding of the sodium-storage mechanism in ternary tin-based chalcogenides.

Declaration of competing interest

The authors declare that they have no known competing financial interests or personal relationships that could have appeared to influence the work reported in this paper.

Acknowledgments

This work was supported by National Natural Science Foundation of China (No. U1832147), Jiangsu Provincial Double-Innovation Doctor Program (No. JSSCBS20210743), Anhui Key Laboratory of low temperature Co-fired Materials (No. 2022LCA04), The Doctor of Suzhou University Scientific Research Foundation Project (No. 2020BS014). The authors also acknowledge the thanks for the great support from the material studio software.

Supplementary materials

Supplementary material associated with this article can be found, in the online version, at doi:10.1016/j.cclet.2023.108552.

References

[1] B. Chen, D.L. Chao, E.Z. Liu, et al., Energy Environ. Sci. 13 (2020) 1096–1131.
[2] Q.B. Yun, L.X. Li, Z.N. Hu, et al., Adv. Mater. 32 (2019) 1903826.
[3] S.D. Luo, S.Y. Dong, C. Lu, et al., J. Colloid Interf. Sci. 513 (2018) 389–399.
[4] X.S. Wang, L. Chang, C.Y. Liu, et al., Electrochim. Acta 318 (2019) 937–948.
[5] X.S. Wang, D. Chen, Z.H. Yang, et al., Adv. Mater. 28 (2016) 8645–8650.
[6] Z.Y. Yi, J.Y. Xu, Z.H. Xu, et al., J. Energy Chem. 60 (2021) 241–248.
[7] S.Q. Zhao, Z.Q. Guo, J. Yang, et al., Small 17 (2021) 2007431.
[8] Y. Wu, Y. Yu, Energy Storage Mater 16 (2019) 323–343.
[9] X. Bian, Y. Dong, D.D. Zhao, et al., ACS Appl. Mater. Interfaces 12 (2020) 3554–3562.
[10] Y.C. Liu, H.Y. Kang, L.F. Jiao, et al., Nanoscale 7 (2015) 1325–1332.
[11] L. Wang, G.R. Yang, S.J. Peng, et al., Energy Storage Mater 25 (2020) 443–476.
[12] Y. Wang, Y.K. Liu, Y.C. Liu, et al., J. Energy Chem. 54 (2021) 225–241.
[13] J. Wang, Z.Z. Wang, J.F. Ni, et al., Energy Storage Mater 45 (2022) 704–719.
[14] Q.T. Tang, H. Su, Y.H. Cui, et al., J. Power Sources 379 (2018) 182–190.
[15] J. Guo, Q.S. Wang, J. Jin, et al., J. Electrochem. Soc. 163 (2016) A654–A659.
[16] Y. Yao, L.C. Zeng, S.H. Hu, et al., Small 13 (2017) 1603513.
[17] Y.C. Liu, N. Zhang, L.F. Jiao, et al., Adv. Mater. 27 (2015) 6702–6707.
[18] Y.C. Liu, N. Zhang, C.M. Yu, et al., Nano Lett. 16 (2016) 3321–3328.
[19] C.H. Wang, B. Zhang, H.F. Xia, et al., Small 16 (2020) 1905853.
[20] C.J. Huang, K.Y. Lin, Y.C. Hsieh, et al., ACS Appl. Mater. Interfaces 13 (2021) 14230–14238.
[21] S.H. Xiao, Z.Z. Li, J.T. Liu, et al., Small 16 (2020) 2002486.
[22] C. Lu, Z.Z. Li, Z. Xia, et al., Nano Res. 12 (2019) 3051–3058.
[23] N. Zhang, Y.C. Liu, Y.Y. Lu, et al., Nano Res. 8 (2015) 3384–3393.
[24] P. Zhang, B. Cao, R.A. Soomro, et al., Chin. Chem. Lett. 32 (2021) 282–285.
[25] D. Chen, X.W. Miao, J. Liu, et al., Chem. Eng. J. 446 (2022) 136772.
[26] Z.L. Cai, Z.L. Peng, X.L. Liu, et al., Chin. Chem. Lett. 32 (2021) 3607–3612.
[27] J. Zhang, Y.C. Liu, H. Liu, et al., Small 16 (2020) 2000504.
[28] T. Wang, Z.X. Huang, D.H. Wang, et al., Chin. Chem. Lett. 34 (2023) 107216.
[29] S.F. Ye, L.F. Wang, F.F. Liu, et al., eScience 1 (2021) 75–84.
[30] F.J. Kong, X.L. He, J.Y. Chen, et al., Energy Technol. 7 (2019) 1900094.
[31] L.J. Zhao, Y. Li, G.Y. Zhou, et al., Chin. Chem. Lett. 32 (2021) 900–905.
[32] J. Guo, J. Yang, J.P. Guan, et al., Chem. Eng. J. 450 (2022) 138007.